*metals*

MDPI

*Article*

# Effect of In Situ TiC Formation and Direct TiN Addition on the Microstructure and Mechanical Properties of CoCrFeNi-Based High-Entropy Alloys

**Zheng Ma [1,2], Jining Guo [2], Tuo Xu [1], Wencheng Zhuang [1] and Zhiqiang Cao [1,*]**

[1] Key Laboratory of Solidification Control and Digital Preparation Technology, School of Materials Science and Engineering, Dalian University of Technology, Dalian 116024, China; mazheng2026@126.com (Z.M.)
[2] College of Control Science and Engineering, Bohai University, Jinzhou 121013, China
* Correspondence: caozq@dlut.edu.cn

**Abstract**

CoCrFeNi-based high-entropy alloys (HEAs) have shown great potential for widespread applications in aerospace, chemical, and medical equipment fields due to their high strength, wear resistance, corrosion resistance, and thermal stability. In the present study, a series of $Ni_2CoCrFeV_xCu_y$ alloys were designed to obtain a ductile FCC matrix suitable for ceramic-particle reinforcement. Subsequently, two representative reinforcement strategies, namely, in situ TiC formation and direct TiN nanoparticle addition, were employed to investigate their effects on the microstructure and mechanical properties of the alloy. The results showed that $Ni_2CoCrFeV_{0.5}Cu_{0.2}$ exhibited the best strength–ductility balance, with a tensile elongation of 51.8% among the designed alloys. Besides, the comprehensive performance of high-entropy alloys can be effectively enhanced by in situ generation of TiC and addition of TiN particles. The in situ synthesized TiC exhibited a finer and more uniform distribution than the directly added TiN particles, resulting in a more favorable strength–ductility balance under the present processing conditions.

**Keywords:** high-entropy alloys; CoCrFeNi-based alloy; in situ synthesis; ceramic reinforcement phase; carbide

## 1. Introduction

High-entropy alloys show excellent comprehensive performance in high-temperature, low-temperature, corrosion, wear, and irradiation resistance [1,2]. As the field of high-entropy alloys continues to evolve, there are increasingly specific requirements regarding various properties, which present new challenges for their design. High-entropy alloys can be categorized into four types by phase composition: CoCrFeNi series dominated by FCC phase, refractory high-entropy alloys dominated by BCC phase, low melting point series, and other series dominated by HCP phase (including rare earths, precious metals, and other elements) [3,4]. Among them, the application of CoCrFeNi high-entropy alloy is more extensive, and the research direction has gradually shifted from the composition design to the process research direction [5–8]. The plasticity of CoCrFeNi high-entropy alloys can be achieved by composition adjustment and process adjustment [9–11], to which the addition of refractory metal elements, such as Nb and Ti, can effectively improve the high-temperature performance of the alloy [9,12–14].

Among various alloying strategies, V and Cu additions have attracted considerable attention in FCC-type CoCrFeNi-based high-entropy alloys. Previous studies have shown

Check for updates

Academic Editor: Seok Su Sohn

Received: 15 April 2026
Revised: 3 June 2026
Accepted: 11 June 2026
Published: 23 June 2026

**Copyright:** © 2026 by the authors. Licensee MDPI, Basel, Switzerland. This article is an open access article distributed under the terms and conditions of the Creative Commons Attribution (CC BY) license.

that moderate V addition can provide solid solution strengthening and lattice distortion strengthening while maintaining relatively good ductility of the FCC matrix [15]. In addition, V can modify the deformation behavior and improve the strength–ductility balance of CoCrFeNi-based alloys [16]. Cu is frequently introduced to FCC high-entropy alloys because of its ability to stabilize the FCC phase and improve plastic deformation compatibility [17–19]. Although Cu segregation may occur during solidification owing to its limited solid solubility, Cu-containing CoCrFeNi-based alloys generally exhibit excellent ductility. Therefore, V and Cu were selected in the present study to develop a ductile FCC matrix alloy suitable for subsequent ceramic-particle reinforcement investigations.

Small-scale ceramic phases are often employed as reinforcing phases due to their ability to enhance solid solution strength and provide precipitation strengthening [1]. To improve the strength and toughness of the alloy, some researchers add ceramic phase, such as rare earth oxides and TiC. The preparation of metal matrix composites can be divided into traditional methods, such as liquid stirring and powder metallurgy, and in situ synthesis methods [20,21]. Li et al. [22] employed laser cladding to fabricate fine microstructured CoCrFeNiMn high-entropy alloys containing TiN, concentrating on the impact of TiN particle reinforcements on the strength and ductility of high-entropy alloys, and found that the majority of TiN particles were distributed at grain boundaries and served as nucleation sites during solidification. Cai et al. [23] synthesized TiC-reinforced FeMnCrNiCo+x(TiC) high-entropy alloys. The fine grains and high dislocation densities enhanced the resistance of the high-entropy alloys. Guo et al. [24] synthesized in situ TiN-reinforced CoCr2FeNiTi high-entropy alloys. In situ processes have been extensively studied due to their straightforward preparation, low production costs, and excellent interfacial bonding [25,26]. TiC exhibits high strength and hardness, making it a commonly utilized reinforcing phase in both traditional alloys and high-entropy alloys [27]. However, in most cases, TiC phase has a granular or rod-like microstructure morphology and is prone to agglomeration, resulting in a significant loss of plasticity of the alloy [28].

In this study, a high-entropy alloy with better plasticity and FCC structure is designed. The effect of V and Cu on the plasticity of the alloy is studied. Additionally, TiC nanophase is generated in the $Ni_2CoCrFeV_xCu_y$ alloy by high-energy ball milling and vacuum melting. In the control group, TiN nanoparticles are added directly to the alloy. The effects of in situ synthesis and direct addition of nanoparticles on the microstructure and mechanical property of the alloy are analyzed.

## 2. Materials and Methods

### *2.1. Material Preparation*

Samples of $Ni_2CoCrFe$ (Shanghai RD-Best New Material Technology Co. Ltd., Shanghai, China) were produced by arc melting pure (>99.5 pct) constituent metals under an argon atmosphere and then casted into a copper mold with the diameter of 45 mm. Each sample had a mass of 100 g. The elemental compositions of the designed alloys are listed in Table 1, and the calculated values of valence electron concentration (VEC), mixing enthalpy ($\Delta H$), and atomic size difference ($\Delta\delta$) among the elements are shown in Table 2. V and Cu were added to the $Ni_2CoCrFe$ alloy to obtain a series of $Ni_2CoCrFeV_xCu_y$ ($x$ = 0.2, 0.5; $y$ = 0.2, 0.4, 0.6, 0.8, 1) alloys (Figure 1a). It tends to form a single-phase FCC solid solution structure when $\delta < 3.75\%$, $-7.27 < \Delta H < 4$, and VEC > 8 [29]. The $Ni_2CoCrFeV_xCu_y$ ($x$ = 0.2, 0.5; $y$ = 0.2, 0.4, 0.6, 0.8, 1) alloy has an FCC-dominated solid solution structure, which meets the design expectations.

**Table 1.** Physical parameters of the constituent elements.

| | Co | Cr | Fe | Ni | V | Cu |
|---|---|---|---|---|---|---|
| atomic radius (A) | 1.12 | 1.28 | 1.26 | 1.24 | 1.34 | 1.28 |
| melting point (°C) | 1495 | 1907 | 1538 | 1455 | 1910 | 1083 |
| crystal structure | HCP<br>FCC | BCC<br>FCC | BCC<br>FCC | FCC | BCC | FCC |

**Table 2.** Calculated VEC, $\Delta H$, and $\Delta\delta$ values of the designed $Ni_2CoCrFeV_xCu_y$ alloys.

| x | y | VEC | $\Delta H$ (KJ/mol) | $\Delta\delta$ (%) |
|---|---|---|---|---|
| 0.2 | 0 | 8.46 | −5.3 | 1.76 |
| | 0.2 | 8.56 | −3.81 | 1.76 |
| | 0.5 | 8.68 | −1.95 | 1.75 |
| | 1 | 8.87 | 0.44 | 1.74 |
| 0.5 | 0 | 8.27 | −0.07 | 2.26 |
| | 0.2 | 8.37 | −5.56 | 2.24 |
| | 0.5 | 8.5 | −3.64 | 2.2 |
| | 1 | 8.69 | −1.14 | 2.14 |

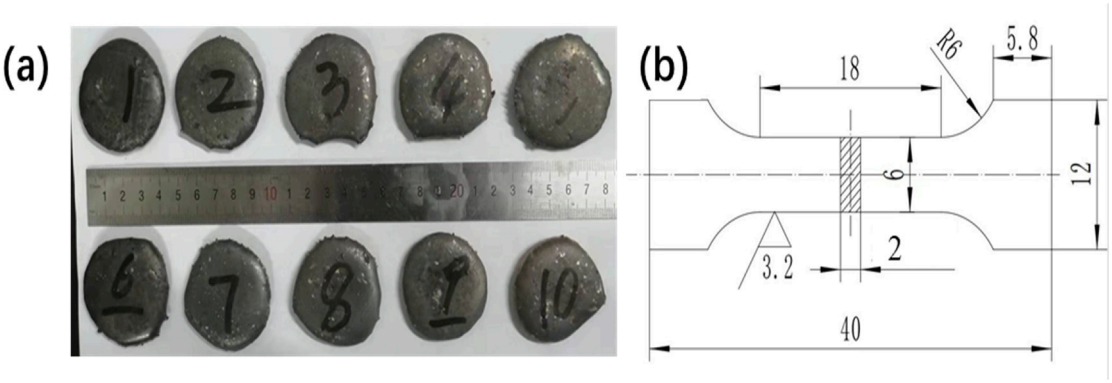



**Figure 1.** Macromorphology of the $Ni_2CoCrFeV_xCu_y$ alloy ingots and tensile specimen geometry: (**a**) as-cast alloy ingots and (**b**) schematic diagram of tensile sample dimensions.

The $Ni_2CoCrFeV_xCu_y$ alloy with the optimal toughness was chosen as the base material for incorporating nanophase. For the $TiC/Ni_2CoCrFeV_xCu_y$ alloy, the 50 μm graphite powder was subjected to ball milling at a speed of 175 r/min for a duration of 8 h using a high-energy ball mill. Then, it was enveloped with Ni foil and placed alongside titanium sponge and Co, Cr, Fe, Ni, V, and Cu metals in a vacuum arc furnace (DHL-400, Sky Technology Development Co., Ltd., Shenyang, China). The melting temperature was set at 2000 °C and maintained for 2 min. For the $TiN/Ni_2CoCrFeV_xCu_y$ alloy, TiN particles with an average size of 40 nm were directly introduced into the vacuum arc furnace and melted together with Co, Cr, Fe, Ni, V, and Cu at a temperature of 2000 °C for 2 min, followed by air cooling.

### *2.2. Microstructural Characterization*

The cylindrical specimens with dimensions of 2 mm in height and 8 mm in diameter were taken from the central region of the ingots. After mechanical polishing, the specimens were cleaned with ethanol. The microstructure of the specimens was analyzed by field-emission scanning electron microscopy/energy-dispersive spectroscopy (FE-SEM/EDS; Regulus 8100, Hitachi, Tokyo, Japan). SEM observations were carried out at an accelerating voltage of 15 kV. Meanwhile, the microstructure of nanocomposite specimens was served by transmission electron microscopy (TEM; JEM-2200FS, JEOL, Tokyo, Japan). Disk specimens

of 3 mm in diameter were punched from the sheets after mechanical polishing to 0.05 mm thick. Foilmens for TEM were prepared by twin-jet electropolishing in the solution of 95% absolute ethanol and 5% perchloric acid (volume%). The chemical composition of the $Ni_2CoCrFeV_xCu_y$ ingots was identified by X-ray diffractometer (XRD; SMARTLAB9, Rigaku, Osaka, Japan). XRD analysis was performed using Cu K$\alpha$ radiation over a 2$\theta$ range of 20–100°.

### *2.3. Mechanical Tests*

Tensile test was carried out on $Ni_2CoCrFeV_xCu_y$ ingots using a universal testing machine (XinSanSi, CMT4305, Shenzhen, China) at room temperature with a strain rate of $1 \times 10^{-3}$ $s^{-1}$. The dimensions of the tensile specimen are shown in Figure 1b. Compression specimens with a length of 10 mm and diameter of 5 mm were taken from the nanocomposite ingots. The compression test was carried out on a universal testing machine (DNS100, Shenyang, China) with a loading speed of 0.6 $mm^{-1}{\cdot}min^{-1}$. The values of yield strength and elongation presented were the average of three measurements.

## 3. Results

### *3.1. Alloy Design*

Since ceramic-particle reinforcement generally increases strength at the expense of ductility, a matrix alloy with high initial plasticity is desirable for retaining adequate ductility after reinforcement addition. Therefore, the $Ni_2CoCrFeV_xCu_y$ alloy system was first optimized to obtain a ductile FCC matrix before introducing ceramic reinforcements.

Figure 2 shows the XRD pattern of the $Ni_2CoCrFeV_xCu_y$ ($x$ = 0.2, 0.5; $y$ = 0.2, 0.4, 0.6, 0.8, 1) alloy with different Cu and V contents. XRD patterns indicate that FCC is the dominant phase in all investigated alloys.

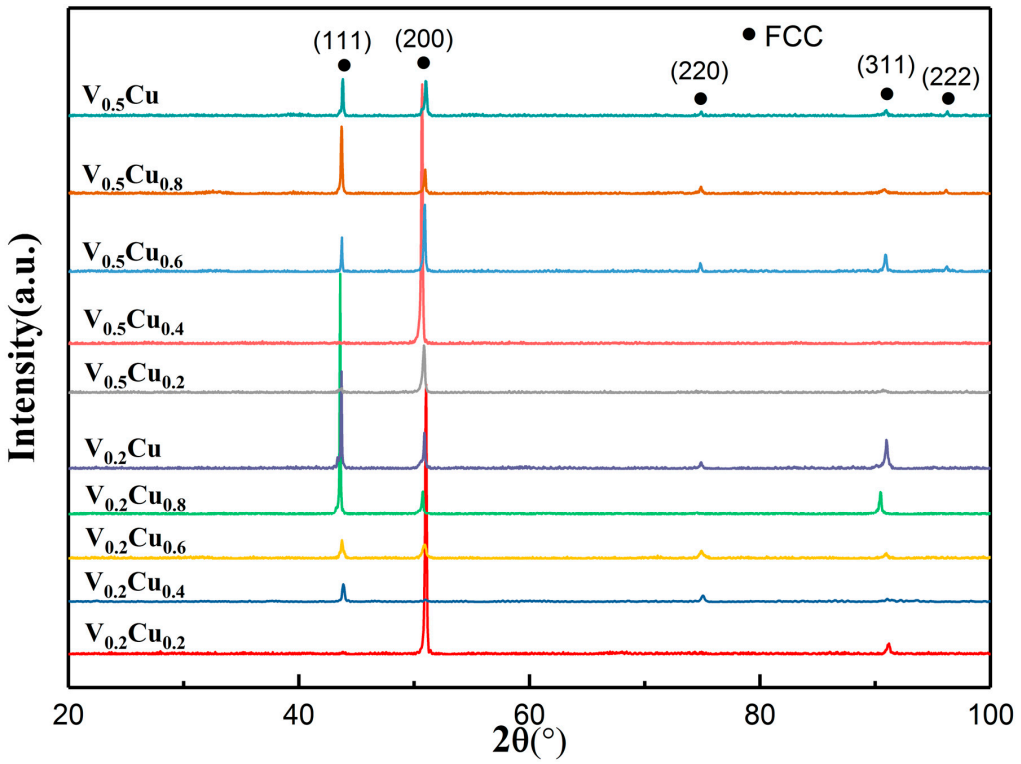



**Figure 2.** XRD pattern of $Ni_2CoCrFeV_xCu_y$ alloys with different V and Cu contents.

Figures 3 and 4 show the SEM microstructure of the cast $Ni_2CoCrFeV_{0.2}Cu_y$ alloy and $Ni_2CoCrFeV_{0.5}Cu_y$ alloy. As the Cu content increased, the accumulation of Cu at the

grain boundary became gradually more pronounced, transitioning from a granular form (Figure 4c, spot A) to a rod-like shape (Figure 4e, spot B).

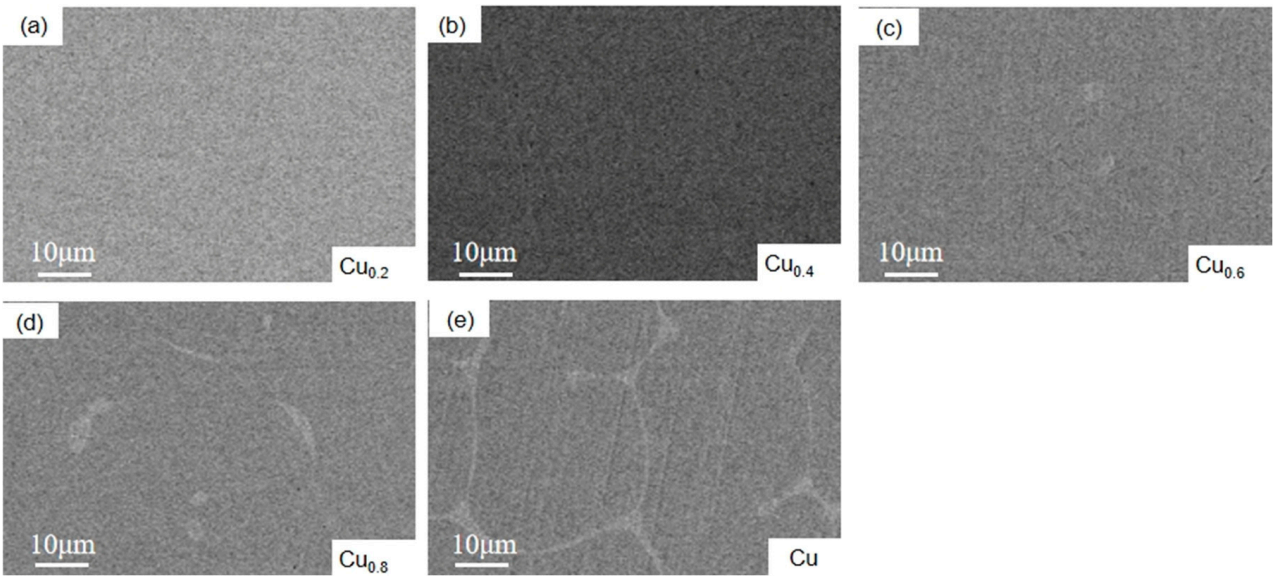



**Figure 3.** SEM microstructure of $Ni_2CoCrFeV_{0.2}Cu_y$ alloys: (**a**) $y$ = 0.2, (**b**) $y$ = 0.4, (**c**) $y$ = 0.6, (**d**) $y$ = 0.8, and (**e**) $y$ = 1.0.

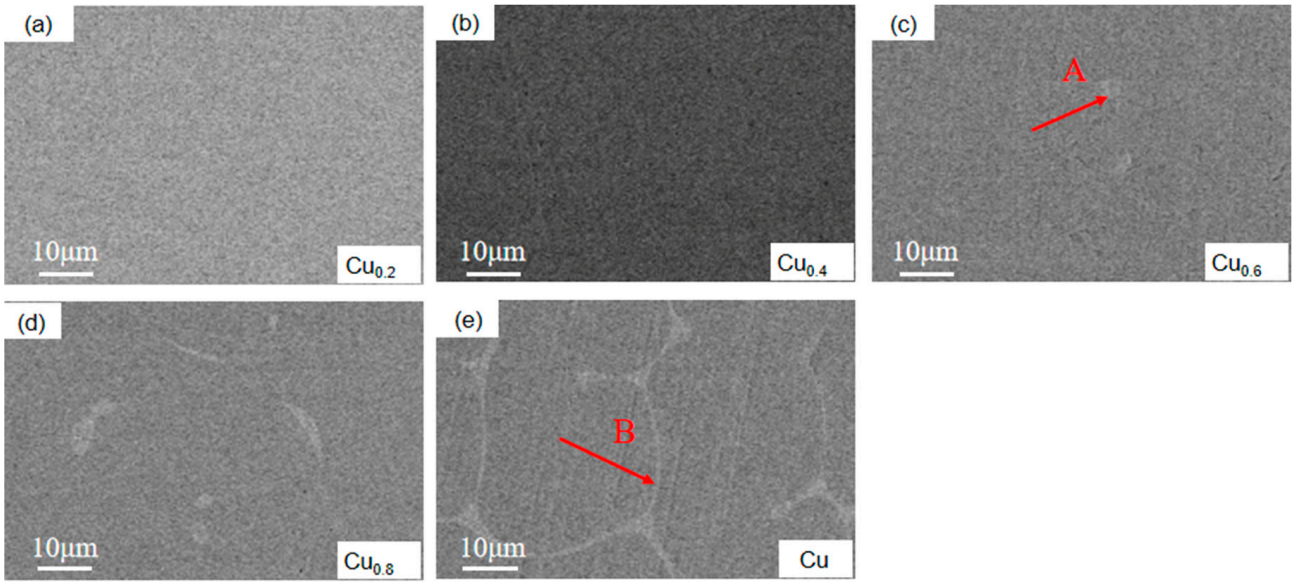



**Figure 4.** SEM microstructure of $Ni_2CoCrFeV_{0.5}Cu_y$ alloys: (**a**) $y$ = 0.2, (**b**) $y$ = 0.4, (**c**) $y$ = 0.6, (**d**) $y$ = 0.8, and (**e**) $y$ = 1.0.

Figure 5 shows the EDS results for the $Ni_2CoCrFeV_{0.5}Cu$ alloy. The distribution of Cu is significantly enriched at the grain boundaries. The compressive stress–strain curve of the alloy is shown in Figure 6. The $Ni_2CoCrFeV_xCu_y$ alloy exhibits excellent tensile elongation, as evidenced by a compression deformation rate exceeding 50% without any occurrence of fracture. Moreover, the yield strength increased with the increase of V and Cu content.

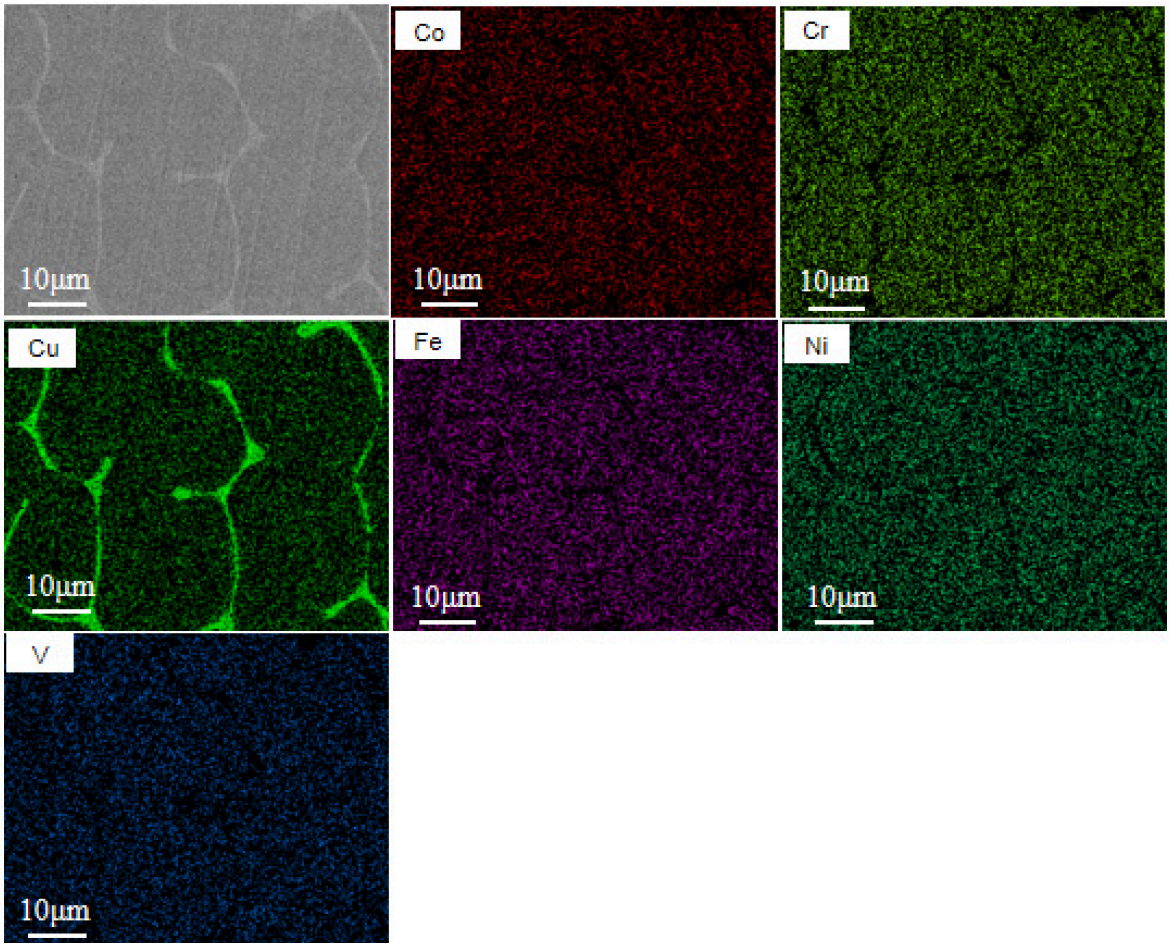



**Figure 5.** EDS elemental mapping of the $Ni_2CoCrFeV_{0.5}Cu$ alloy.

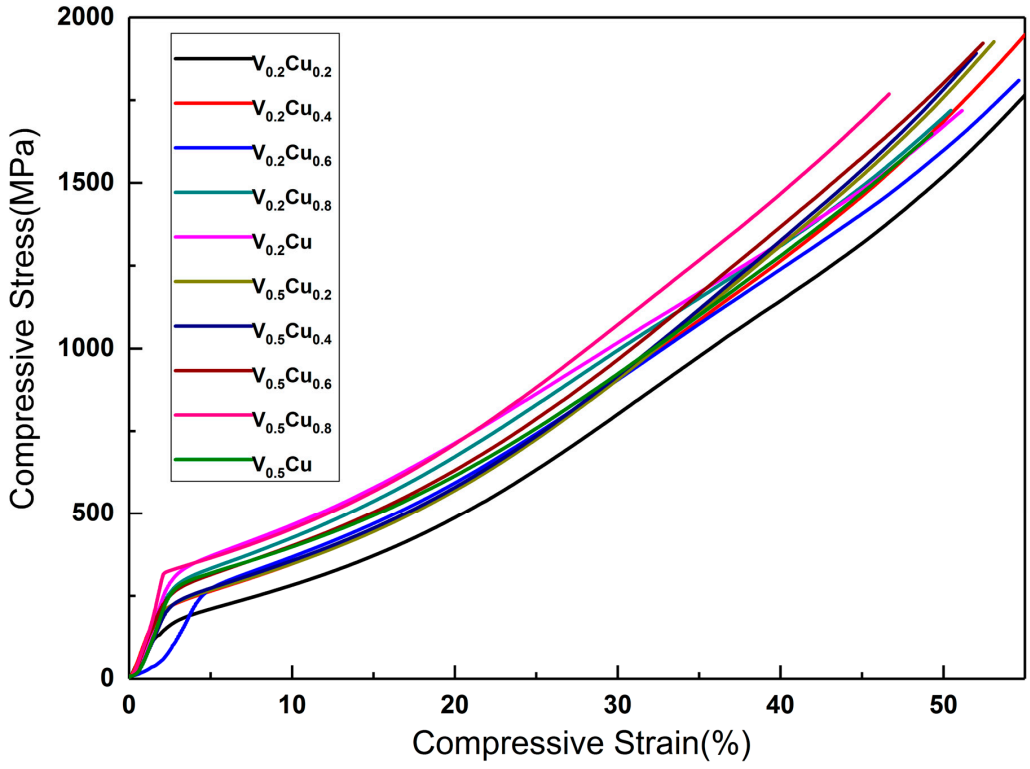



**Figure 6.** Compressive stress–strain curve of $Ni_2CoCrFeV_xCu_y$ alloys with different V and Cu contents.

The tensile stress–strain curve of the alloy is shown in Figure 7. The $Ni_2CoCrFeV_{0.5}Cu_{0.2}$ alloy exhibits superior plasticity, with a tensile strength of 494.1 MPa and an elongation of 51.8%. Consequently, $Ni_2CoCrFeV_{0.5}Cu_{0.2}$ was chosen as the matrix material for nanocomposites.

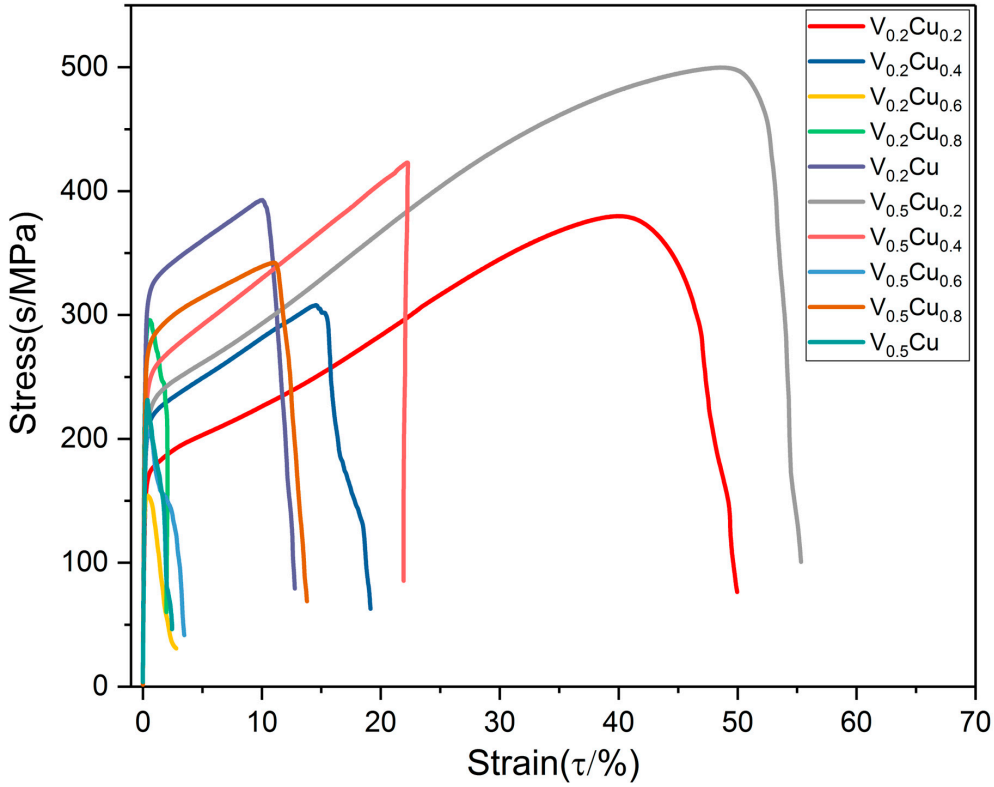



**Figure 7.** Tensile stress–strain curve of $Ni_2CoCrFeV_xCu_y$ alloys with different V and Cu contents.

The tensile fracture morphology of the $Ni_2CoCrFeV_{0.5}Cu_{0.2}$ alloy is depicted in Figure 8, revealing an abundance of dimples indicative of ductile fracture behavior. The macroscopic fracture morphology exhibits a typical cup–cone pattern characterized by fibrous features (Figure 8a), while the microscopic fracture morphology displays a honeycomb structure (Figure 8b, spot A).

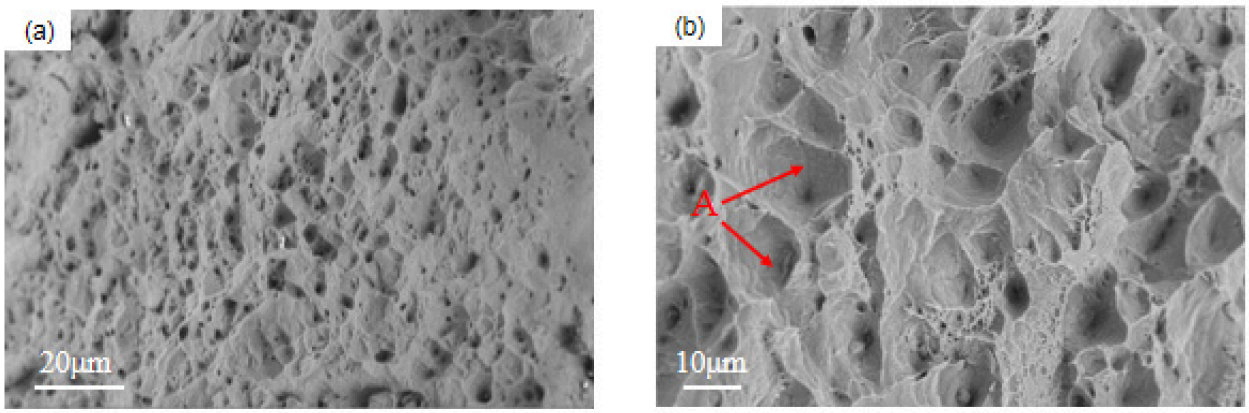



**Figure 8.** Tensile fracture morphology of the $Ni_2CoCrFeV_{0.5}Cu_{0.2}$ alloy: (**a**) 200× and (**b**) 800×, spot A represents a honeycomb structure fracture surface.

### 3.2. Microstructure and Mechanical Property of the TiC/$Ni_2CoCrFeV_{0.5}Cu_{0.2}$ Alloy

Figure 9 shows the XRD patterns of Ni2CoCrFe$V_{0.5}Cu_{0.2}$ alloys with TiC contents of 1.5, 3, and 6 (wt.%). The addition of TiC did not alter the phase composition of the high-entropy alloy. With an increase in TiC content, a diffraction peak corresponding to TiC emerges in the diffraction pattern and its intensity gradually intensifies. This observation indicates that the TiC/$Ni_2CoCrFeV_{0.5}Cu_{0.2}$ high-entropy alloy maintains the crystal structure of FCC while generating in situ reinforcement from TiC.

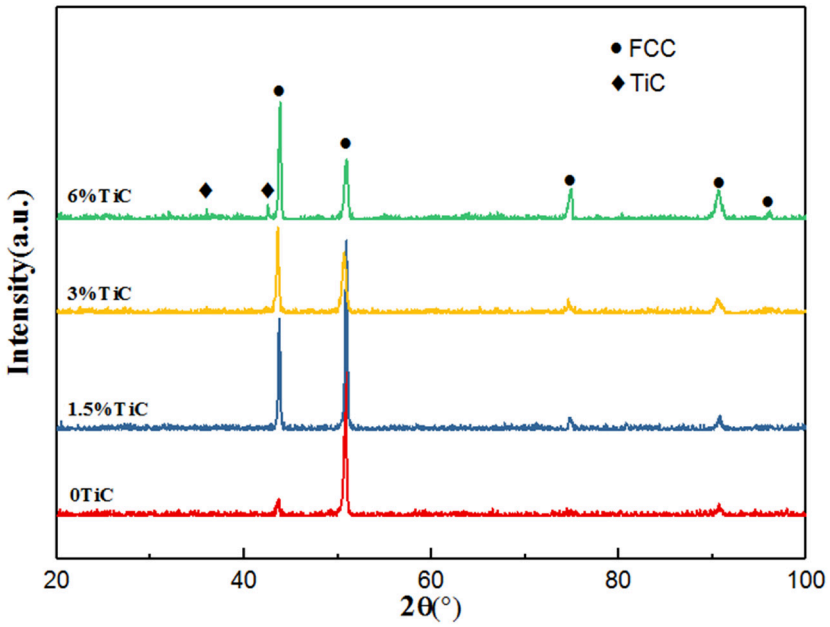



**Figure 9.** XRD pattern of TiC/$Ni_2CoCrFeV_{0.5}Cu_{0.2}$ alloys with different TiC contents.

Figure 10 shows the microstructure photographs of the TiC/$Ni_2CoCrFeV_{0.5}Cu_{0.2}$ alloy. When the TiC content is 1.5 wt.%, as illustrated in Figure 10a–c, TiC particles predominantly appear as small spheres or regular blocks, evenly distributed within the grains, with sizes of 5–7 μm. TEM observations reveal the presence of spherical and massive (Ti,V)C-reinforcing phases at the grain boundaries, as shown in Figure 11. This phenomenon can be attributed to the high melting point of TiC, which precipitates first during the solidification process of the matrix and serves as a heterogeneous nucleation site that refines the grain size of the composite and enhances its overall properties. Most fine spherical strengthening phases are uniformly distributed along the grain boundaries.

As the TiC content increases to 3 wt.%, as illustrated in Figure 10d–f, the amount of TiC significantly rises, with some TiC accumulating at the grain boundaries and adopting a rod-like morphology, thereby enveloping the grain boundaries. As the TiC content increases to 6 wt.%, as illustrated in Figure 10g–i, distinct TiC aggregates and a limited number of micropores are observed at the grain boundaries. The micropores primarily result from the removal of TiC aggregates from the treated surface during sample processing.

The EDS analysis of the precipitate (spot A), grain boundary (spot B), and matrix (spot C) in Figure 10 is shown in Table 3. In the $Ni_2CoCrFeV_{0.5}Cu_{0.2}$ alloy with different contents of TiC, the distribution pattern of elements is essentially uniform. The precipitates primarily consist of Ti and C, along with a minor amount of V. The elements at position B are dominated by Ti, V, and C, and there is no obvious segregation that exists in the matrix.

Figure 12 shows the tensile stress–strain curve of the TiC/$Ni_2CoCrFeV_{0.5}Cu_{0.2}$ alloy. With the increase of the reinforcing phase TiC, the alloy demonstrates an increase in tensile

strength and a decrease in elongation. This is attributed to the addition of the Ti-reinforcing phase, which exerts strengthening effects.

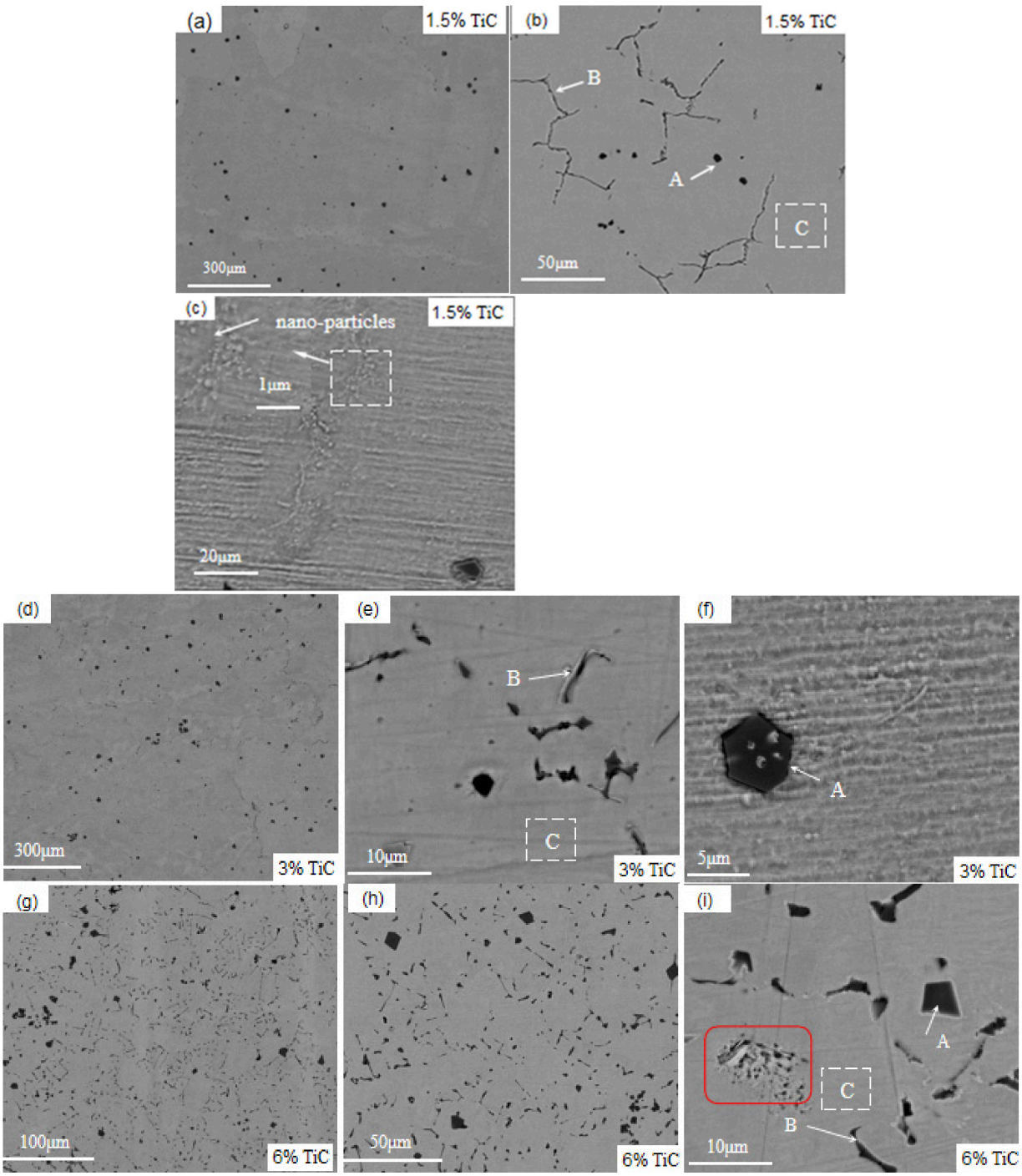



**Figure 10.** SEM microstructure of TiC/$Ni_2CoCrFeV_{0.5}Cu_{0.2}$ alloys with different TiC contents: (**a**–**c**) 1.5 wt.% TiC, (**d**–**f**) 3 wt.%TiC, and (**g**–**i**) 6 wt.% TiC. The labels A, B, and C indicate the positions selected for EDS analysis, and the corresponding chemical compositions are listed in Table 3. The white dashed boxes mark representative regions selected for local observation or EDS analysis, while the red box in (i) highlights a region with pronounced TiC agglomeration.

**Table 3.** EDS analysis of different regions in the TiC/$Ni_2CoCrFeV_{0.5}Cu_{0.2}$ alloy shown in Figure 10 (at%).

| | | Co | Cr | Fe | Ni | V | Cu | Ti | C |
|---|---|---|---|---|---|---|---|---|---|
| 1.5%TiC | A | 0.84 | 1.37 | 0.83 | 1.48 | 1.40 | 0.00 | 45.42 | 48.66 |
| | B | 3.07 | 4.85 | 3.16 | 6.24 | 14.66 | 0.89 | 16.75 | 50.36 |
| | C | 14.50 | 14.09 | 14.71 | 28.58 | 6.75 | 3.45 | 0.70 | 17.21 |
| 3%TiC | A | 1.81 | 3.03 | 1.93 | 3.35 | 10.96 | 0.29 | 22.96 | 55.67 |
| | B | 1.89 | 3.52 | 2.06 | 3.53 | 14.06 | 0.28 | 18.7 | 55.95 |
| | C | 14.29 | 14.38 | 14.73 | 27.68 | 7.00 | 3.84 | 2.02 | 16.06 |
| 6%TiC | A | 1.60 | 2.41 | 1.88 | 2.74 | 11.05 | 0.00 | 31.49 | 48.83 |
| | B | 1.66 | 3.16 | 1.68 | 2.79 | 13.25 | 0.02 | 24.97 | 52.47 |
| | C | 14.90 | 13.84 | 15.48 | 27.96 | 6.17 | 3.09 | 1.98 | 16.58 |

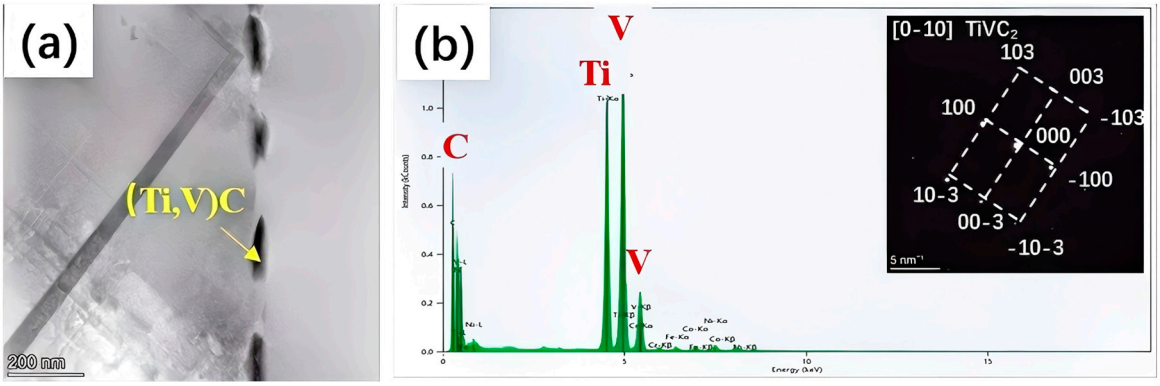



**Figure 11.** TEM microstructure of 1.5 wt.% TiC/$Ni_2CoCrFeV_{0.5}Cu_{0.2}$ alloys: (**a**) nanoscale (Ti,V)C precipitate at the grain boundary, and (**b**) corresponding EDS spectrum and selected area electron diffraction (SAED) pattern of the precipitate marked in (**a**).

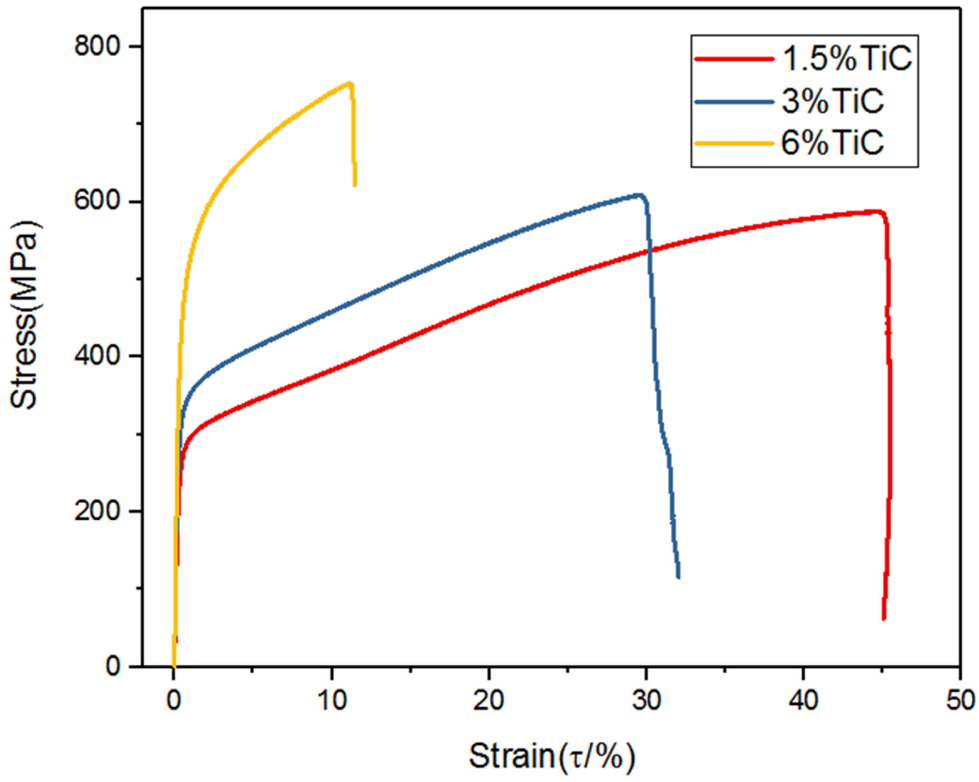



**Figure 12.** Tensile stress–strain curve of TiC/$Ni_2CoCrFeV_{0.5}Cu_{0.2}$ alloys with different TiC contents.

### *3.3. Microstructure and Mechanical Property of the TiN/$Ni_2CoCrFeV_{0.5}Cu_{0.2}$ Alloy*

TiN nanoparticles with different contents were added into the matrix alloy $CrCoFeNi_2V_{0.5}Cu_{0.2}$ to analyze the change rule of alloy physical phase and organization and morphology, as well as the enhancement mechanism of TiN on the alloy and principle.

Figure 13 shows the XRD patterns of $Ni_2CoCrFeV_{0.5}Cu_{0.2}$ alloys with TiN contents of 1.5, 3, and 6 (wt.%), which shows that similar to the addition of TiC, the addition of TiN did not change the phase composition of the high-entropy alloy. With the increase of the reinforcing phase TiN, the diffraction peaks corresponding to TiN appeared in the XRD patterns, and the number and intensity of the diffraction peaks gradually increased with the increasing TiN content. Finally, the high-entropy alloy matrix composites with simple solid solution as a matrix and TiN as a reinforcing phase were obtained.

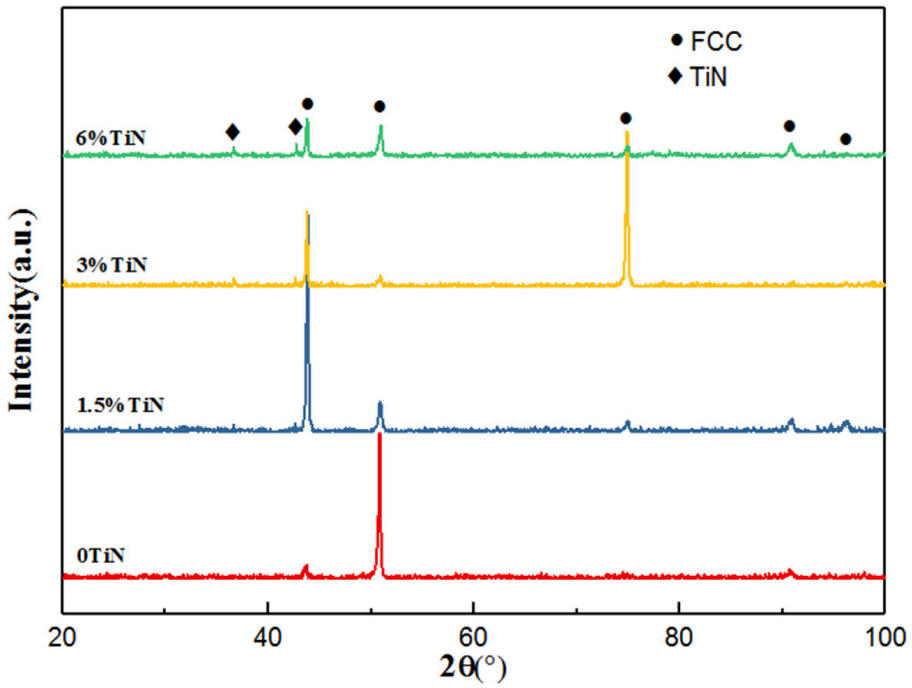



**Figure 13.** XRD pattern of TiN/$Ni_2CoCrFeV_{0.5}Cu_{0.2}$ alloys with different TiN contents.

Figure 14 shows the microstructure of the TiN/$CrCoFeNi_2V_{0.5}Cu_{0.2}$ alloy. At a TiN content of 1.5 wt.% (Figure 14a,b), TiN particles exhibit irregular angular shapes and are evenly distributed within the grain boundaries, with sizes of approximately 7 μm. TEM observations revealed a nano-(Ti,V)N precipitated phase, as shown in Figure 15, characterized by a cubic morphology. Due to its high melting point, TiN precipitates first during the solidification of the matrix and subsequently acts as a heterogeneous nucleation site during the solidification process of the matrix alloy, which can refine the grain size of the composite. However, no precipitates were observed in samples containing 6% TiN, indicating that agglomeration of TiN nanoparticles occurred.

As the TiN content increases to 3 wt.%, as illustrated in Figure 14c,d, both the quantity and size of TiN particles increase significantly. When the TiN content reaches 6 wt.%, a substantial aggregation of TiN particles is observed, as shown in Figure 14e,f.

The EDS analysis of the precipitate (spot A), grain boundary (spot B), and matrix (spot C) in Figure 13 is shown in Table 4. The composition of the precipitates is predominantly Ti and N, with a minor amount of V dissolved in the solid solution. In the dendrite position B, the principal elements are Ti and N, along with a small quantity of V. Although N and V are also very easy to react to form VN, the affinity is smaller than that between Ti and V and it is not easy to replace the N in the TiN to generate VN. In the sample with 6%

TiN, there exists a distinct microscale enrichment of TiN at grain boundaries, as attested by EDS analysis, which is primarily TiN. This phenomenon substantiates that a considerable amount of TiN is agglomerated at grain boundaries, validating the conclusion that no nanoscale TiN was detected in the TEM analysis (Figure 15).

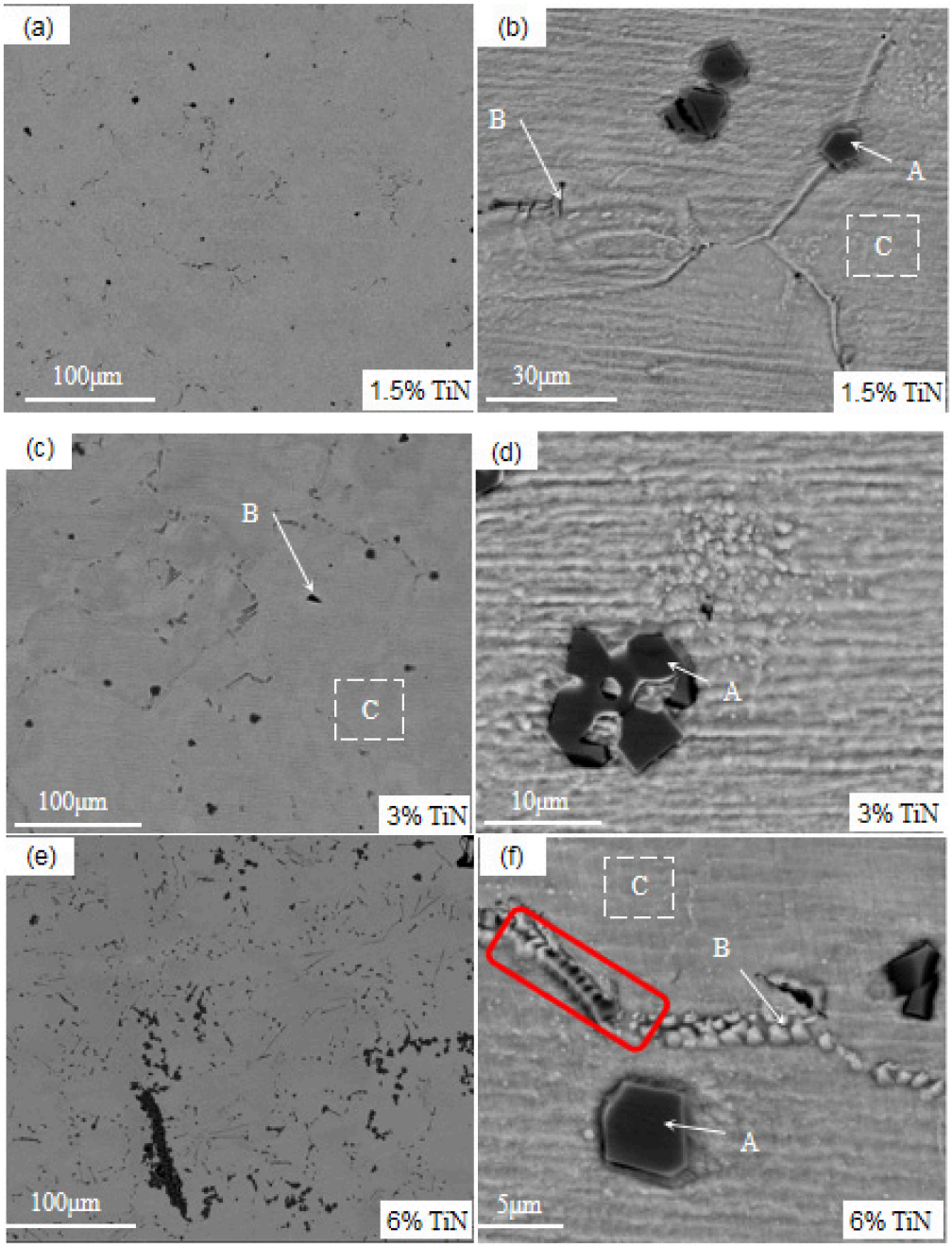



**Figure 14.** SEM microstructure of TiN/$Ni_2CoCrFeV_{0.5}Cu_{0.2}$ alloys with different TiN contents: (**a**,**b**) 1.5 wt.% TiN, (**c**,**d**) 3 wt.% TiN, and (**e**,**f**) 6 wt.%TiN. The labels A, B, and C indicate the positions selected for EDS analysis, and the corresponding chemical compositions are listed in Table 4. The white dashed boxes mark representative regions selected for local observation or EDS analysis, while the red box in (**f**) highlights a region with pronounced TiN agglomeration.

Figure 16 shows the tensile stress–strain curve of the TiN/$Ni_2CoCrFeV_{0.5}Cu_{0.2}$ alloy. With the increase of the reinforcing phase TiN, the alloy demonstrates decreases in tensile strength and elongation. This is attributed to the agglomeration of nano-TiN particles forming micron-sized impurities, which actually reduces the strength of the alloy.

**Table 4.** EDS analysis of different regions in the TiC/$Ni_2CoCrFeV_{0.5}Cu_{0.2}$ alloy shown in Figure 14 (at%).

| | | Co | Cr | Fe | Ni | V | Cu | Ti | N |
|---|---|---|---|---|---|---|---|---|---|
| 1.5%TiN | A | 0 | 0 | 0 | 0.58 | 12.33 | 0 | 36.24 | 50.84 |
| | B | 0.17 | 0.63 | 0.18 | 0.33 | 10.16 | 0.01 | 29 | 43.35 |
| | C | 14.31 | 14.67 | 14.55 | 28.01 | 7.15 | 3.81 | 0.23 | 17.28 |
| 3%TiN | A | 0 | 0 | 0 | 0.36 | 6.05 | 0 | 41.99 | 51.06 |
| | B | 8.53 | 7.46 | 8.22 | 15.98 | 5.9 | 1.43 | 15.71 | 36.75 |
| | C | 14.59 | 14.3 | 14.3 | 28.48 | 6.83 | 3.38 | 0.26 | 17.41 |
| 6%TiN | A | 0.81 | 0.86 | 0.86 | 1.25 | 6.2 | 0 | 42.02 | 21 |
| | B | 0.52 | 0 | 0 | 0.99 | 0.77 | 0 | 39.4 | 52.31 |
| | C | 14.9 | 14.6 | 14.2 | 28.7 | 6.76 | 3.61 | 0.76 | 16.48 |

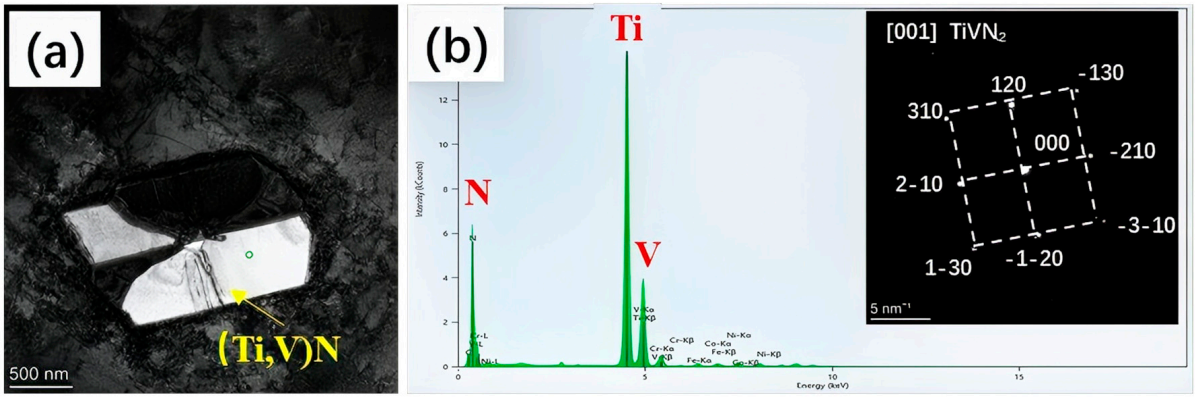



**Figure 15.** TEM characterization of the 1.5 wt.% TiN/$Ni_2CoCrFeV_{0.5}Cu_{0.2}$ alloy: (**a**) nanoscale (Ti,V)N precipitate in the matrix, and (**b**) corresponding EDS spectrum and SAED pattern of the precipitate marked in (**a**).

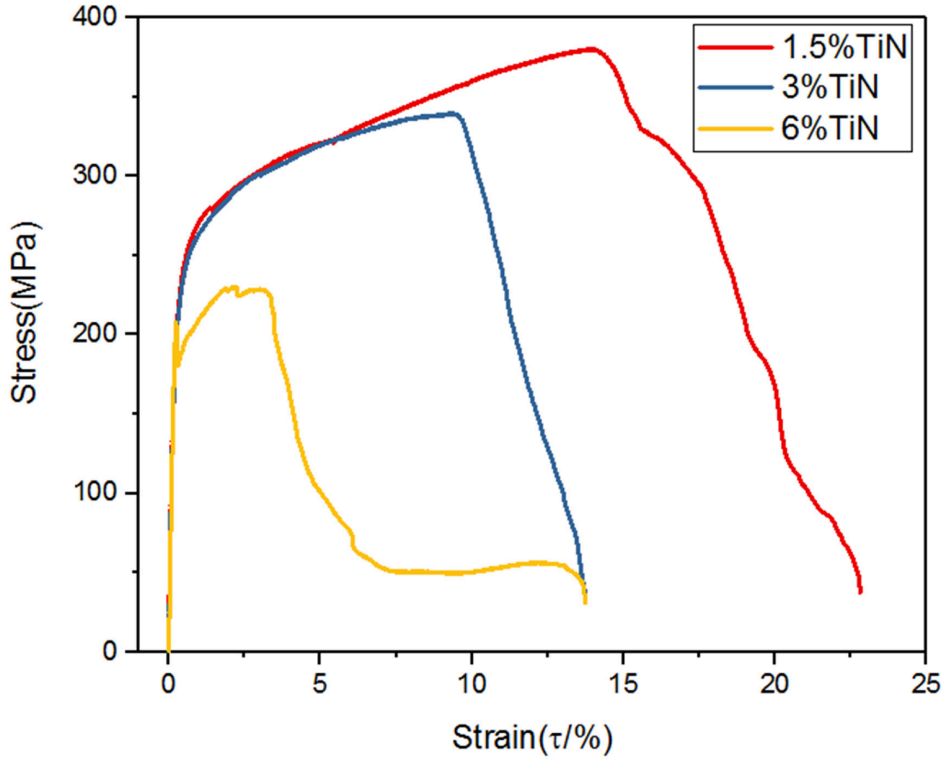



**Figure 16.** Tensile stress–strain curve of TiN/$Ni_2CoCrFeV_{0.5}Cu_{0.2}$ alloys with different TiN contents.

## 4. Discussion

### *4.1. In Situ Synthesis Process of TiC with Different Morphologies*

Thermodynamic and XRD analyses show that TiC phase can exist stably in TiC/$Ni_2CoCrFeV_{0.5}Cu_{0.2}$ composites. When TiC content is low, the size of precipitated TiC in the composite material becomes smaller. As the TiC content increases, there is a significant increase in the proportion of bulk and rod-shaped TiC.

Different in situ synthesis pathways of TiC-reinforced phases lead to the formation of reinforced phases with different morphologies. There are two in situ synthesis pathways: one involves the conversion of intermediate compounds into phases within the high-entropy alloy melt, while the other entails the dissolution of elements and their subsequent direct contact reaction to form an enhanced phase. Due to the limited diffusion capability of elements in the high-entropy alloy melt, reinforcements obtained through the first pathway tend to retain the morphology of ternary compounds, whereas those obtained through the second pathway exhibit a finer size.

The TiC reinforcement phase of the TiC/$Ni_2CoCrFeV_{0.5}Cu_{0.2}$ composite alloy has three forms, which are spherical, massive polygon, and nanoparticles. By spectral composition analysis, the tiny spherical phase (shown as A in Figure 10b) is obtained by the reaction between Ti and C atoms in the molten state. The reinforced phase of TiC particles is dominated by the elements Ti and C, with trace amounts of V. The in situ autogenous synthesis process is the direct reaction between Ti and C to obtain the TiC-reinforced phase, which can be considered as the end product of the in situ autogenous synthesis reaction for the TiC phase of the solid solubilized trace element V. The TiC phase can be regarded as the final product of the in situ autogenous synthesis reaction.

The nano-TiC-reinforced phase is generated during the cooling process of the composite melt, again due to the in situ autogenous synthesis process for Ti and C obtained by direct reaction. The presence of nano-TiC at grain boundaries primarily results from the solid solubility of Ti and C elements in the alloy. During the solid–liquid coexistence phase, Ti and C atoms along the solid–liquid interface are excluded from the liquid phase. When their concentration reaches a critical level, fine tic-enhanced phases precipitate. Ultimately, nano-TiC-enhanced phases appear at the final solidified grain boundaries.

The content of V in TiC particles exhibits a significant increase, which is further supported by TEM analysis. The presence of (Ti, V)C is due to the cubic crystal structures of both TiC and VC, as well as their similar atomic radii. According to Hume–Rothery's law, TiC and VC can form an enhanced phase of (Ti, V)C within an infinite solid solution. However, no (Ti,V)C diffraction peaks are seen in the XRD pattern, which may be due to the relatively low content of C and the preferential reaction with Ti, resulting in the low content of V produced.

### *4.2. Improvement of Mechanical Properties of Alloys by Enhancement Phase*

The mixing enthalpy between elements is calculated as Equation (1) [30]:

$$\Delta H_{mix} = \sum_{i=1,i\neq j}^{n} \Omega_{ij} c_i c_j,\ \Omega_{ij} = \sum_{i=1,i\neq j}^{n} 4\Delta_{mix}^{AB}. \quad (1)$$

Here, $\Delta_{mix}^{AB}$ is the liquid mixing enthalpy of the *AB* binary alloy, and $c_i$ and $c_j$ are the atomic percentages of component i and component j, respectively.

The calculated values in Table 5 reveal that the mixing enthalpy of Ti and C elements is negative, indicating the potential formation of TiC ceramic particles in situ. Meanwhile, the addition of TiN results in the most negative mixing enthalpies for Ti and N, while the mixing enthalpies for Cr, V, and other elements are comparatively smaller. At a specific

temperature, an increase in TiN content leads to the formation of interstitial solid solutions, while the remaining portion precipitates nitride particles.

**Table 5.** Binary mixing enthalpy between the constituent elements in the designed alloy system (kJ/mol).

| Δ*H* | Co | Cr | Fe | Ni | V | Cu | N | Ti |
|---|---|---|---|---|---|---|---|---|
| Co | - | −4 | −1 | 0 | −14 | 6 | −75 | −28 |
| Cr | | - | −1 | −7 | −2 | 12 | −107 | −7 |
| Fe | | | - | −2 | −7 | 13 | −87 | −17 |
| Ni | | | | - | −18 | 4 | −69 | −35 |
| V | | | | | - | 5 | −143 | −2 |
| Cu | | | | | | - | −84 | −9 |
| C | | | | | | | | −109 |
| N | | | | | | | | −190 |

The in situ synthesized TiC reinforcement resulted in alloys with better tensile strength and tensile elongation than those reinforced with externally added TiN nanoparticles. This is due to the in situ synthesized TiC-reinforced phase having better matrix wettability and high interfacial bonding strength, while the addition of TiN nanoparticles had poor matrix wettability, resulting in low interfacial bonding strength. The nanoparticles are very easy to agglomerate, when added to the 6 wt.%, and even appeared in the "chain" agglomeration, thus making the alloy toughness significantly reduced.

When the TiC content reaches 1.5 wt.%, the enrichment of TiC at grain boundaries plays the role of grain boundary reinforcement; at the same time, the TiC nanoparticles precipitated on the grain boundaries play the role of connectivity, making the TiC strength on the grain boundaries higher, so the tensile strength of the alloy increases as the amount of TiC added increases. However, the amount of TiC on the grain boundary increases significantly, which makes the grain boundary size larger, cutting the continuity of the alloy, and making the linkage between the grains decrease, which is detrimental to the performance of the alloy. The 1.5% TiC composite alloy has a tensile strength of about 593 MPa, which compared with the matrix increased by 20%, while the tensile rate is still up to 45%.

## 5. Conclusions

In this study, the strength and toughness of the $Ni_2CoCrFe$ high-entropy alloy were enhanced by incorporating an appropriate content of Cu and V. Nanocomposites were prepared by incorporating TiN nanoparticles or in situ synthesizing a TiC nano-reinforced phase with $Ni_2CoCrFeV_xCu_y$ serving as the matrix. The effects of the in situ synthesis method and direct addition method on the microstructure of the alloy were compared and analyzed. The main conclusions are as follows:

(1) By adjusting the alloy composition and added elements, a high-entropy alloy with good plasticity and FCC structure was successfully designed and prepared. The $Ni_2CoCrFeV_{0.5}Cu_{0.2}$ alloy was found to have excellent mechanical properties and was selected as the matrix for ceramic-particle reinforcement treatment.

(2) The in situ reaction between Ti and C successfully generated TiC-containing reinforcement phases in the $Ni_2CoCrFeV_{0.5}Cu_{0.2}$ alloy. Different TiC morphologies, including fine spherical particles, polygonal particles, and nanoscale precipitates, were observed. The formation of these morphologies is likely associated with local solidification conditions and compositional evolution during the in situ reaction process. Excessive TiC addition pro-

moted particle coarsening and agglomeration, which may adversely affect the mechanical properties of the composites.

(3) Compared with the TiN-added composites, the in situ synthesized TiC composites exhibited a more favorable strength–ductility balance under the present processing conditions.

**Author Contributions:** Conceptualization, Z.C.; methodology, Z.M. and J.G.; software, T.X.; validation, T.X. and W.Z.; formal analysis, T.X.; investigation, Z.M. and J.G.; resources, Z.C.; data curation, Z.M., J.G., and T.X.; writing—original draft, Z.M.; writing—review and editing, Z.C.; visualization, J.G. and W.Z.; supervision, W.Z.; project administration, W.Z.; funding acquisition, Z.C. All authors have read and agreed to the published version of the manuscript.

**Funding:** This work was financially supported by the National Natural Science Foundation of China (Grant Number 52271024).

**Data Availability Statement:** The original contributions presented in this study are included in the article. Further inquiries can be directed to the corresponding author.

**Conflicts of Interest:** The authors declare no conflicts of interest.

## References

1. Miracle, D.B.; Senkov, O.N. A critical review of high entropy alloys and related concepts. *Acta Mater.* **2017**, *122*, 448–511. [CrossRef]
2. Chuang, M.-H.; Tsai, M.-H.; Wang, W.-R.; Lin, S.-J.; Yeh, J.-W. Microstructure and wear behavior of AlxCo1. 5CrFeNi1. 5Tiy high-entropy alloys. *Acta Mater.* **2011**, *59*, 6308–6317. [CrossRef]
3. Fan, J.; Yao, H.W.; Pu, J.B. Research progress and prospect of wear corrosion properties of high entropy alloy coatings. *Surf. Eng. China* **2025**, *38*, 1–23.
4. Zhou, Z. Progress in research and application of high entropy alloy in laser additive repai. *Metall. Mater.* **2024**, *44*, 145–147.
5. Dąbrowa, J.; Kucza, W.; Cieślak, G.; Kulik, T.; Danielewski, M.; Yeh, J.-W. Interdiffusion in the FCC-structured Al-Co-Cr-Fe-Ni high entropy alloys: Experimental studies and numerical simulations. *J. Alloys Compd.* **2016**, *674*, 455–462. [CrossRef]
6. Zhou, Y.; Zhang, Y.; Kim, T.; Chen, G. Microstructure characterizations and strengthening mechanism of multi-principal component AlCoCrFeNiTi 0.5 solid solution alloy with excellent mechanical properties. *Mater. Lett.* **2008**, *62*, 2673–2676. [CrossRef]
7. Lee, D.-H.; Seok, M.-Y.; Zhao, Y.; Choi, I.-C.; He, J.; Lu, Z.; Suh, J.-Y.; Ramamurty, U.; Kawasaki, M.; Langdon, T.G.; et al. Spherical nanoindentation creep behavior of nanocrystalline and coarse-grained CoCrFeMnNi high-entropy alloys. *Acta Mater.* **2016**, *109*, 314–322. [CrossRef]
8. Liu, W.H.; Wu, Y.; He, J.Y.; Nieh, T.G.; Lu, Z.P. Grain growth and the Hall–Petch relationship in a high-entropy FeCrNiCoMn alloy. *Scr. Mater.* **2012**, *68*, 526–529. [CrossRef]
9. Uporov, S.; Estemirova, S.; Bykov, V.; Zamyatin, D.; Ryltsev, R. A single-phase ScTiZrHf high-entropy alloy with thermally stable hexagonal close-packed structure. *Intermetallics* **2020**, *122*, 106802. [CrossRef]
10. Laplanche, G.; Berglund, S.; Reinhart, C.; Kostka, A.; Fox, F.; George, E. Phase stability and kinetics of σ-phase precipitation in CrMnFeCoNi high-entropy alloys. *Acta Mater.* **2018**, *161*, 338–351. [CrossRef]
11. Kauffmann, A.; Stüber, M.; Leiste, H.; Ulrich, S.; Schlabach, S.; Szabó, D.V.; Seils, S.; Gorr, B.; Chen, H.; Seifert, H.-J.; et al. Combinatorial exploration of the High Entropy Alloy System Co-Cr-Fe-Mn-Ni. *Surf. Coat. Technol.* **2017**, *325*, 174–180. [CrossRef]
12. Shun, T.; Chang, L.; Shiu, M. Microstructures and mechanical properties of multiprincipal component CoCrFeNiTi x alloys. *Mater. Sci. Eng. A* **2012**, *556*, 170–174. [CrossRef]
13. Ping, Z.L. Study on Forming and Properties of High Entropy Alloy/Ceramic Composite Lattice Structures. Master's Thesis, China Mining University, Xuzhou, China, 2023.
14. Zhou, R.; Chen, G.; Liu, B.; Wang, J.W.; Han, L.L.; Liu, Y. Microstructures and wear behaviour of (FeCoCrNi)1–x(WC)x, high entropy alloy composites. *Int. J. Refract. Met. Hard Mater.* **2018**, *75*, 56–62. [CrossRef]
15. Hu, M.; Jiang, X.; Dong, M.; Hu, M.; Yang, Y. Preparation and effect of vanadium addition on the mechanical properties of CoCrFeNiVx high-entropy alloy. *J. Mater. Res. Technol.* **2023**, *27*, 7705–7712. [CrossRef]
16. Shen, R.; Ni, Z.; Peng, S.; Yan, H.; Tian, Y. Effects of V Addition on the Deformation Mechanism and Mechanical Properties of Non-Equiatomic CoCrNi Medium-Entropy Alloys. *Material* **2023**, *16*, 5167. [CrossRef]
17. Zheng, H.; Chen, R.; Qin, G.; Li, X.; Su, Y.; Ding, H.; Guo, J.; Fu, H. Maicrostructure evolution, Cu segregation and tensile properties of CoCrFeNiCu high entropy alloy during directional solidification. *J. Mater. Sci. Technol.* **2020**, *38*, 19–27. [CrossRef]

18. Huang, L.; Wang, X.; Huang, B.; Zhao, X.; Chen, H.; Wang, C. Effect of Cu segregation on the phase transformation and properties of AlCrFeNiTiCux high-entropy alloys. *Intermetallics* **2022**, *140*, 107397. [CrossRef]
19. Otto, F.; Dlouhý, A.; Somsen, C.; Bei, H.; Eggeler, G.; George, E.P. The influences of temperature and microstructure on the tensile properties of a CoCrFeMnNi high-entropy alloy. *Acta Mater.* **2013**, *61*, 5743–5755. [CrossRef]
20. Zhang, X.Y.; Li, J.L.; Ci, J.W.; Huo, H.L.; Yang, Y.F.; Yang, J.J.; Li, J.; Ren, P.; Chen, D.X.; Zhang, P.; et al. Research progress of laser cladding ceramic particle reinforced metal matrix composites. *Therm. Spray. Technol.* **2024**, *16*, 18–34.
21. Li, P.Y. Preparation of carbon nanotube reinforced metal matrix composites by powder metallurgy: Advances and challenges. *Aeronaut. Manuf. Technol.* **2023**, *66*, 14–35.
22. Li, B.; Qian, B.; Xu, Y.; Liu, Z.; Xuan, F. Fine-structured CoCrFeNiMn high entroy alloy matrix composite with 12 wt% TiN particle reinforcements via selective laser melting assisted additive manufacturing. *Mater. Lett.* **2019**, *252*, 88–91. [CrossRef]
23. Cai, Y.; Zhu, L.; Cui, Y.; Shan, M.; Li, H.; Xin, Y.; Han, J. Fracture and wear mechanisms of FeMnCrNiCo+x(TiC) composite high entroy alloy cladding layers. *Appl. Surf. Sci.* **2021**, *543*, 148794. [CrossRef]
24. Guo, Y.; Shang, X.; Liu, Q. Microstructure and properties of in-situ TiN reinforced lasercladding CoCrzFeNiTix high entroy alloy composite coatings. *Surf. Coat. Technol.* **2018**, *344*, 353–358. [CrossRef]
25. Yao, C.-Z.; Zhang, P.; Liu, M.; Li, G.-R.; Ye, J.-Q.; Liu, P.; Tong, Y.-X. Electrochemical preparation and magnetic study of Bi–Fe–Co–Ni–Mn high entropy alloy. *Electrochim. Acta* **2008**, *53*, 8359–8365. [CrossRef]
26. Andreoli, A.F.; Shuleshova, O.; Witusiewicz, V.T.; Wu, Y.; Yang, Y.; Ivashko, O.; Dippel, A.C.; Zimmermann, M.V.; Nielsch, K.; Kaban, I. In situ study of non-equili-brium solidification of CoCrFeNi high-entropy alloy and CrFeNi and CoCrNi ternary suballoys. *Acta Mater.* **2021**, *212*, 116880. [CrossRef]
27. Liu, H.X.; Chen, J.; Yang, C.; Liu, Y.X.; Wang, Y.Y.; Hao, X.H. Structural characteristics and high temperature oxidation resistance of in-situ autogenic Ti-Al-B functional coating by laser cladding. *J. Kunming Univ. Sci. Technol. (Nat. Sci. Ed.)* **2024**, *49*, 42–54.
28. Chen, R.R.; Chen, X.G.; Gao, X.F.; Qin, G.; Song, Q.; Cui, H.Z. Microstructure and mechanical properties of CoCrFeNi high entropy alloy enhanced by in-situ authigenic carbide. *Mater. Rev.* **2022**, *36*, 27–32.
29. Jiang, L.; Lu, Y.; Jiang, H.; Wang, T.; Wei, B.; Cao, Z.; Li, T. Formation rules of single phase solid solution in high entropy alloys. *Mater. Sci. Technol.* **2016**, *32*, 587–592. [CrossRef]
30. Takeuchi, A.; Inoue, A. Classification of bulk metallic glasses by atomic size difference, heat of mixing and period of constituent elements and its application to characterization of the main alloying element. *Mater. Trans.* **2005**, *46*, 2817–2829. [CrossRef]


**Disclaimer/Publisher's Note:** The statements, opinions and data contained in all publications are solely those of the individual author(s) and contributor(s) and not of MDPI and/or the editor(s). MDPI and/or the editor(s) disclaim responsibility for any injury to people or property resulting from any ideas, methods, instructions or products referred to in the content.